Journal of Nanobiotechnology

RESEARCH

Open Access

Neutrophil membrane-derived nanoparticles protect traumatic brain injury via inhibiting calcium overload and scavenging ROS

Hongqing Li[1†], Duo Sun[1†], Zhenghuan Zhao[2], Jingqin Fang[3], Muyao Li[2], Chaoqun Lv[4], Weicheng Zhou[1], Ning Li[1], Yu Guo[5], Zhile Cao[5], Kaijun Liu[4*] and Xiao Chen[1*]

Abstract

The secondary injury is more serious after traumatic brain injury (TBI) compared with primary injury. Release of excessive reactive oxygen species (ROS) and Ca^{2+} influx at the damaged site trigger the secondary injury. Herein, a neutrophil-like cell membrane-functionalized nanoparticle was developed to prevent ROS-associated secondary injury. NCM@MP was composed of three parts: (1) Differentiated neutrophil-like cell membrane (NCM) was synthesized, with inflammation-responsive ability to achieve effective targeting and to increase the retention time of Mn_3O_4 and nimodipine (MP) in deep injury brain tissue via C-X-C chemokine receptor type 4, integrin beta 1 and macrophage antigen-1. (2) Nimodipine was used to inhibit Ca^{2+} influx, eliminating the ROS at source. (3) Mn_3O_4 further eradicated the existing ROS. In addition, NCM@MP also exhibited desirable properties for T_1 enhanced imaging and low toxicity which may serve as promising multifunctional nanoplatforms for precise therapies. In our study, NCM@MP obviously alleviated oxidative stress response, reduced neuroinflammation, protected blood–brain barrier integrity, relieved brain edema, promoted the regeneration of neurons, and improved the cognition of TBI mice. This study provides a promising TBI management to relieve the secondary spread of damage.

Keywords Traumatic brain injury, Reactive oxygen species, Neutrophil membrane, Mn_3O_4, Nimodipine

[†]Hongqing Li and Duo Sun have contributed equally to this work.

*Correspondence:
Kaijun Liu
kliu_tmmu@126.com
Xiao Chen
xiaochen229@foxmail.com
Full list of author information is available at the end of the article

Graphical Abstract

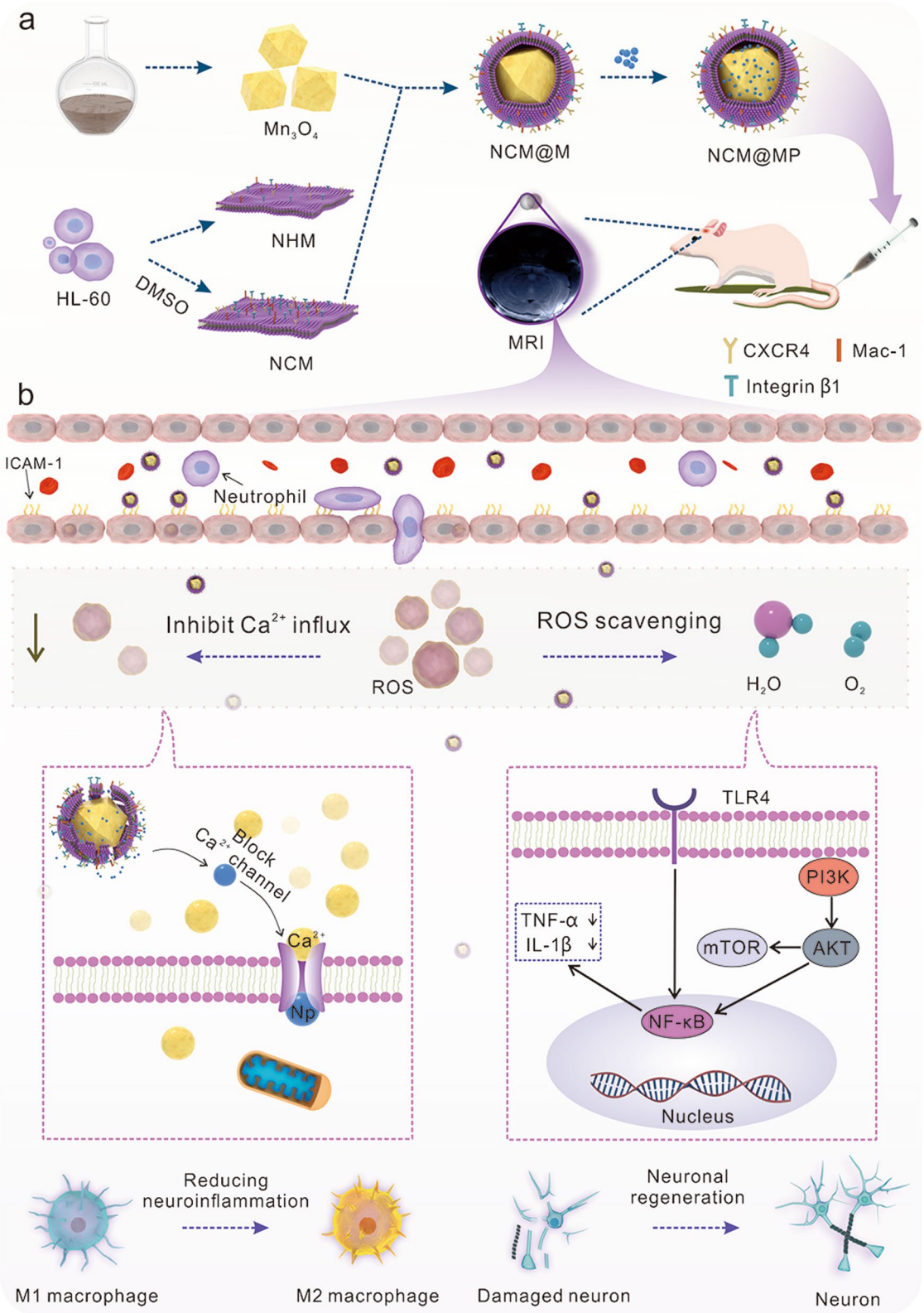

Introduction

Traumatic brain injury (TBI) results in life-threatening consequences, such as irreversible neurological dysfunction and in-hospital deaths [1]. TBI is classified into primary and secondary injury based on the underlying pathophysiological mechanism. Secondary injury is considered to be more severe and capable of causing acute and chronic cellular and organ damages [2]. It's potential to improve clinical outcomes that implementing interventions to mitigate secondary injury. The secondary injury encompasses a range of cellular and molecular changes which are interrelated and give rise to uncontrolled reactive oxygen species (ROS) release in TBI. The rapid and excessive influx of calcium into the cytoplasm is a prominent factor in initiating ROS generation [3]. Moreover, the interactions between excessive calcium influx and ROS overproduction can form a positive feed forward, which further aggravates cell damage [4, 5]. Therefore, calcium overload inhibition combines with ROS scavenging may bring new breakthrough for TBI therapy.

Nimodipine has been shown to be neuroprotective in the patients with aneurysmal subarachnoid haemorrhage [6] and has been expected to treat TBI by inhibiting calcium overload as a calcium channel blocker [5]. Apart from Ca^{2+} influx, various endogenous and exogenous substances tend to collectively produce ROS. Mn_3O_4 nanoparticles (NPs) have gained increasing attention for their excellent ROS scavenging ability [7]. Mn_3O_4 NPs exhibit a range of enzyme-like activities and considerable efficacy in scavenging the superoxide radical (O^{2-}) and hydroxyl radical (·OH). Moreover, these NPs display superior stability compared to natural enzyme counterparts in vitro and effectively mitigate ROS-induced inflammation in mice [8]. Furthermore, Mn_3O_4 NPs possess desirable characteristics for enhanced magnetic resonance imaging (MRI) [9]. Hence, Mn_3O_4 NPs combined with nimodipine could exert better effects, aiming to mitigate the levels of ROS to prevent secondary injury as well as be used for precise imaging. Unfortunately, oral administration or intravenous drip constricts the effective concentration of nimodipine in the cerebrospinal fluid and elevated dosage of nimodipine may increase the risk of hypotension [6]. As for above reasons, an effective drug delivery system targeting to the vulnerable regions of the brain needs to be developed.

The presence of the blood–brain barrier (BBB) poses a constraint on achieving an effective drug concentration in TBI conditions. Consequently, there is a pressing need for BBB-crossing protectants with enhanced ROS-scavenging capabilities. One possible way is to enhance the targeting ability and biosafety of nanomaterials through cell membrane encapsulation. Neutrophils can migrate towards areas of inflammation, traverse blood vessels and infiltrate into tissues to carry out their functions [10]. The adhesion of neutrophils to the endothelium involves several leukocyte integrins, namely lymphocyte function-associated antigen-1 (CD11a/CD18), macrophage-1 antigen (Mac-1), and very late antigen-4 (VLA-4), which interact with their respective endothelial ligands, intercellular adhesion molecule 1 (ICAM-1) and vascular cell adhesion molecule 1 (VCAM-1) [11]. C-X-C chemokine receptor 4 (CXCR4) promotes inflammation by driving neutrophils migrate into inflammatory region [12]. The potential effects of neutrophil-membrane-encased Mn_3O_4 and nimodipine, which scavenge ROS, have rarely been demonstrated.

In order to capitalize on the unique molecular-mediated inflammatory tendency, we have modified neutrophils to overexpress integrin beta 1, Mac-1, and CXCR4 on their membranes. These modified neutrophil membranes (NCM) were utilized to coat Mn_3O_4 and nimodipine (MP) to produce NCM@MP. We hypothesized that NCM@MP presented the following remarkable advantages: (1) NCM utilized the inflammatory tendencies of CXCR4, integrin beta 1 and Mac-1 as fuels for delivery of the nanozymes to achieve effective targeting and to increase their retention time in the injury brain areas, which simultaneously complete the nanozymes-mediated therapy in time; (2) Nimodipine owned a superior activity to eliminate TBI-induced harmful substances including excessive ROS/Ca^{2+} and inflammatory cytokines by nimodipine; (3) Mn_3O_4 could further eradicate the existing ROS and protect mice from ROS-induced secondary injuries in vivo. In addition, Mn_3O_4 served as promising multifunctional nanoplatforms for MRI and treatment (Graphic for manuscript). This study provides new strategy for the treatment of TBI to prevent secondary spread of damage.

Results and discussion

Synthesis and characterization of NCM@MP

The structure and physical features of Mn_3O_4 NPs were detected by transmission electron microscope (TEM) in Fig. 1a, and the as-obtained Mn_3O_4 NPs with a uniform size ~ 25 nm were shown in Fig. 1d. As shown in Fig. 1b, the lattice shown in TEM agreed well with $d_{[101]} = 0.492$ nm, demonstrating the highly crystalline nature of the as-prepared Mn_3O_4 NPs. The presence of Mn and O elements in the Mn_3O_4 was further verified by the high-angle annular dark field scanning transmission electron microscopy (HAADF-STEM), combining with energy dispersive X-ray (EDX) spectroscopy mapping (Fig. 1c). The X-ray Diffraction (XRD) pattern of Mn_3O_4 NPs was shown in Fig. 1e. All of the measured diffraction peaks matched well with the standard pattern

of naumannite Mn_3O_4 [JCPDS card No. 01–080-0382], confirming their high crystallinity. As catalytic reactions happened on the surface of NPs, the surface of Mn_3O_4 NPs was further characterized by X-ray photoelectron spectroscopy (XPS) (Fig. 1f). Mn $2p_{3/2}$ and $2p_{1/2}$ peaks were centered at 641.7 eV and 653.4 eV, respectively.

HL-60 cells can be stimulated and differentiated by 1.3% DMSO for 4–6 days and then exhibit higher responsiveness to inflamed regions recruitment [13]. They roll, adhere, and crawl better through the BBB due to specific expression of cell membrane proteins [13]. In order to produce nanomaterials that interact with the BBB after intravenous delivery, we first identified proteins that bind to vascular endothelial cell constituents. Figure S1 showed that 1.3% DMSO stimulated HL-60 expressed the targeted proteins, including CXCR4, Integrin beta 1 and MAC-1. Figure 1g verified that these nanovesicles, which gained from stimulated HL-60 cells, possessed the source cell membrane features. Unlike HL-60 cell membrane (NHM), NCM expressed more above-mentioned proteins. In addition, NCM@MP showed difference on targeted protein expressions compared with NHM, but no effect on total expression compared with NCM (Figure S2).

The TEM images of NCM@MP were shown in Fig. 1h. Dynamic light scattering (DLS) measurements revealed that the resulting NCM@MP (Fig. 1i) had an average particle size of ~ 78.8 nm, which was ~41 nm greater than that of the untreated Mn_3O_4 (Fig. 1d). And the zeta potential of NCM@MP was −7.54 mV, which was more negative than that of Mn_3O_4 (Figure S3). Furthermore, according to the standard adsorption curve of free nimodipine (Figure S4), the loading amount of nimodipine on NCM@Mn_3O_4 was about 30.5% (w/w). Additionally, NCM@MP kept strong UV absorptions as free nimodipine (Figure S5). The high loading efficiency of Mn in NCM@MP and stability inspired us to investigate the feasibility of NCM@MP to be an MRI contrast agent. We further measured the relaxivity 1 (r1), and relaxivity 2 (r2) of NCM@MP (Fig. 1j–m) and Mn_3O_4 (Figure S6) by 7.0 T MRI. Relaxation time 1 weighted imaging (T1WI) and relaxation time 2 weighted imaging (T2WI) showed significant contrast enhancement in a concentration-dependent manner (Fig. 1j, k). The r1 and r2 values were 1.5 and 7.8 mM^{-1} s^{-1}, respectively (Fig. 1l, m). These results indicated that NCM@MP could be a promising T1-T2 dual-modal contrast agent with high performance. Based on these above results, NCM@MP had been successfully produced.

The capability of anti-oxidative stress response, anti-inflammatory and neuroprotective function of NCM@MP in vitro

To investigate whether NCM@MP could be uptake by microglia, we cocultured BV2 microglia with NCM@MP. Numerous brown particles were shown in BV2 cells with 50 μg mL^{-1} NCM@MP. TEM showed that nanomaterials were found to be incorporated into endosome-like structures in the cytoplasm (Figure S7, Supporting Information). These findings indicated efficient uptake of NCM@MP by BV2 cells. To evaluate the ROS scavenging ability of nanoparticles on BV2, we assessed the scavenging behavior of different constituents with varied concentrations from 5 to 100 μg mL^{-1} toward $\cdot O^{2-}$, DPPH and ·OH in Supplementary Figure S8. We found that NCM@MP showed stronger scavenging ability than NCM@Mn_3O_4 at 100 μg mL^{-1} but no difference at lower concentrations. As shown in Fig. 2a–c, both MP and NCM@MP showed similar ROS scavenging ability. This indicated that the membrane encapsulation did not compress the activity of the nanophase. NCM@MP scavenged approximately 80% of $\cdot O^{2-}$, 20% of the DPPH, and 30% of ·OH when the concentration was 50 μg mL^{-1}. Considering the hemolysis activity of NCM@MP at 100 μg mL^{-1} (Figure S9), we chose 50 μg mL^{-1} for experiments in vitro. To investigate the scavenging capacity against intracellular ROS, we used a 2,7-dichlorofluorescein diacetate (DCFH-DA) reagent assay kit. The results showed that ROS was significantly increased in lipopolysaccharide (LPS)-triggered BV2 microglia cells, compared with the control (Fig. 2d). NCM@MP scavenged nearly 70% ROS at the concentration of 50 μg mL^{-1}, which was better than NCM@Mn_3O_4. Superoxide dismutase (SOD) is an antioxidant enzyme that removes superoxide anions and protects cells from free radical damage [14]. Malondialdehyde (MDA) presents the degree of lipid peroxidation in cells [15]. Both are important indicators to evaluate cellular oxidative stress. SOD has been reported to effectively clear ROS and relieve inflammation [16].

(See figure on next page.)

Fig. 1 **a** TEM images of Mn_3O_4. **b** The lattice of Mn_3O_4 shown in TEM. **c** HAADF-STEM-EDX mapping of Mn_3O_4. **d** Dynamic light scattering (DLS) measurements of Mn_3O_4. **e** X-ray Diffraction (XRD) pattern of Mn_3O_4. **f** Mn $2p_{1/2}$ and Mn $2p_{3/2}$ XPS spectra of Mn_3O_4. **g** Representative western blot images of Integrin beta 1, MAC-1 and CXCR4, respectively. **h** TEM image of NCM@MP. **i** Dynamic light scattering (DLS) of NCM@MP. **j**–**k** The insets were the corresponding T1WI and T2WI of NCM@MP solution, respectively. **l**–**m** r1 and r2 relaxivity of NCM@MP at the different concentrations of Mn. Data were mean ± SD (n = 3 per group). *$p < 0.05$, **$p < 0.01$, ***$p < 0.001$, ****$p < 0.0001$

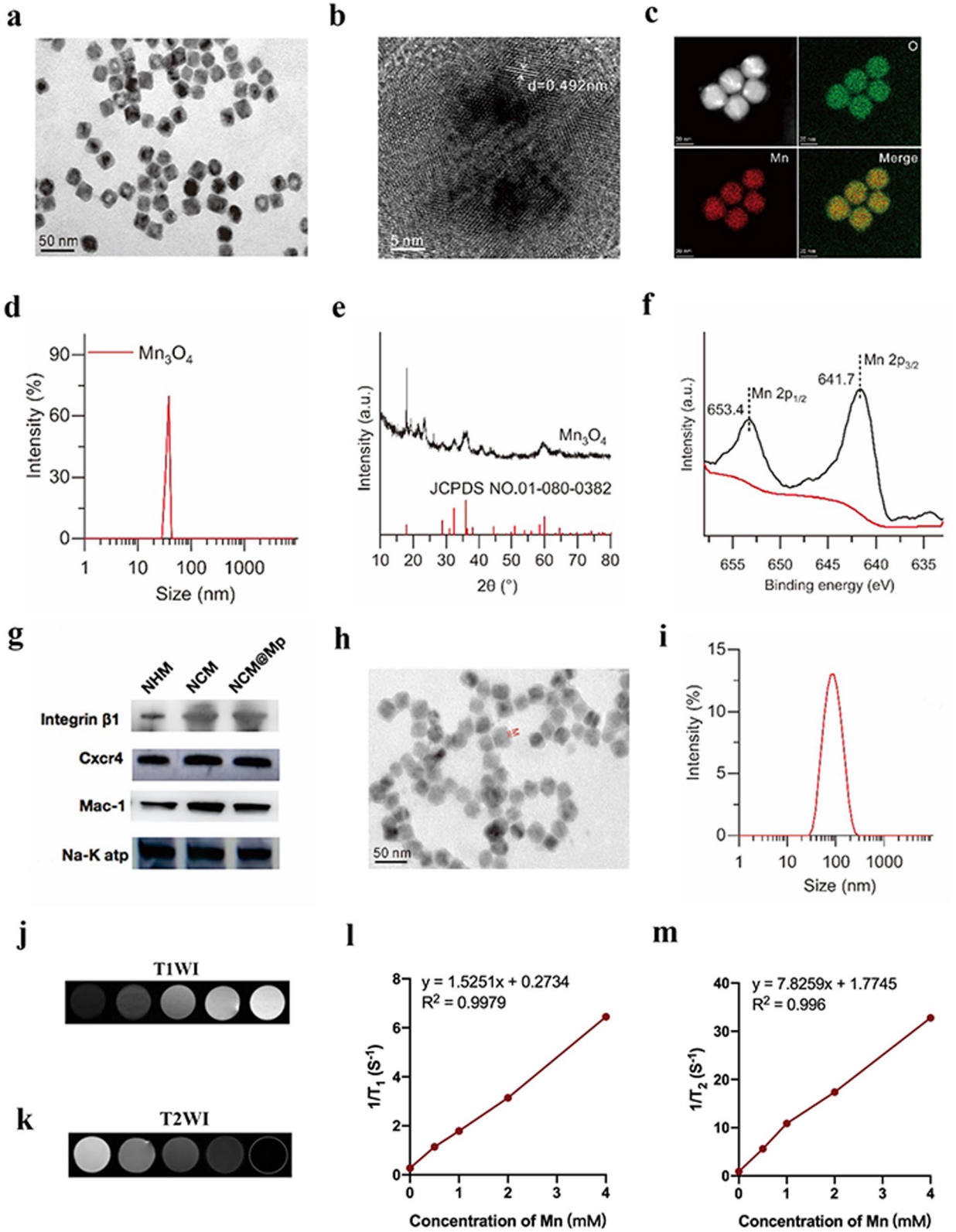

Fig. 1 (See legend on previous page.)

Thus, we detected the SOD and MDA levels of BV2 following LPS intervention and NCM@MP incubation. NCM@MP showed significant benefits in increasing SOD activity and reducing MDA levels (Fig. 2e, f). All above findings indicated the broad-spectrum anti-oxidative capacity of NCM@MP, and the combined functional moieties of MP contributed more to scavenging ROS. ROS can stimulate BV2 microglia cells to produce pro-inflammatory cytokines and some inflammatory mediators [17]. And ROS blockage could reduce interleukin-1β (IL-1β) induced by LPS [18]. The effect of nanoparticles on the production of IL-1β and tumor necrosis factor-α (TNF-α) in BV2 cells was detected by enzyme-linked immunosorbent assay (ELISA) (Fig. 2g, h). LPS dramatically increased the production of IL-1β and TNF-α, compared with the control. NCM@MP significantly decreased the production of these pro-inflammatory cytokines in LPS-induced cells. On the other hand, it has been reported that TBI mediated mitochondrial dysfunction leading to excessive influx of calcium, which triggers secondary injury of TBI [19]. We tested the level of calcium and NCM@MP significantly decreased the degree of calcium overloading in LPS-triggered BV2 cells, as shown in Fig. 2i.

As activated microglia mediated ROS production and increase of neuronal apoptosis [20], we imitated oxidative stress-induced brain injury in vitro by incubating SH-SY5Y cells with H_2O_2 and evaluated the protective effect of NCM@MP. As shown in Fig. 2j–l, H_2O_2 dramatically decreased cell viability resulting from oxidative stress. NCM@MP could efficiently protect cells from excessive ROS-induced damage, in accordance with the findings of their excellent ROS scavenging capability.

MRI and targeting capability of NCM@MP in vitro and in vivo

CXCR4 is involved in the process of inflammation [21], which mediates immune cells migrating into the inflammatory region [22]. Mac-1 was shown to induce ICAM1-dependent receptor-mediated transcytosis across the BBB. It has been used to increase the central nervous system-penetrance of various cargo from small drugs to nanoparticle-based systems [23] which could improve the therapeutic efficacy of the drugs. Thus, it is essential to investigate whether modification of CXCR4/Mac-1 could help the NPs crossing BBB and accumulating in the TBI lesion. To further evaluate the BBB-crossing capability of NCM@MP, we constructed an in vitro model mimicking the nanoparticles passing through the BBB with Transwell system (Fig. 3a). Moreover, disruption of the BBB was induced by adding $CoCl_2$ as previously reported [24]. The results showed that the in vitro BBB crossing efficiency of NCM@MP was 1.5 times higher than that of NHM@MP in the damaged BBB model (Fig. 3b).

To assess the nano-drug delivery and accumulation in TBI lesions, in vivo MRI was conducted [1]. Positive contrast enhancement on T1WI was found after NCM@MP injection (Fig. 3d). At 10 min post injection, T1 relaxation times (Fig. 3c) in TBI lesions were shortened significantly. Then, at 5 h post-injection, relaxation time achieved a minimum of ≈ 60%. At 24 h post-injection, T1 relaxation times gradually regained 97%. These findings suggested the selective TBI lesion accumulation of NCM@MP. We compared the T1 relaxation times of MRI in the TBI lesion between NCM@MP and MP groups at 5 h post-injection (Fig. 3e). These results showed that T1 relaxation times in the TBI lesion were obviously shorter in the NCM@MP group, compared with the MP group (Fig. 3f). These findings suggested that NCM@MP exhibited higher TBI lesion accumulation than MP. The high brain lesion accumulation capability encouraged us to propel NCM@MP into therapeutic efficacy studies for brain injury in vivo.

Therapeutic efficacy of NCM@MP on TBI mouse model

On the basis of the favorable antioxidative, anti-inflammatory activity and advantageous biodistribution of NCM@MP, we investigated its therapeutic efficacy on TBI mouse model. We successfully established TBI model in mice by controlled cortical impact (CCI) as previously reported [24, 25]. Injury area was investigated by triphenyltetrazolium chloride (TTC) staining, which was one of the best immediate tissue staining techniques for TBI confirmation [26]. Compared with the TBI group, NCM@MP treatment exhibited fewer injury area percentage at day-1 post-TBI (Fig. 4a, b). Massive BBB disruption resulting from TBI and followed brain

(See figure on next page.)

Fig. 2 **a** $\cdot O^{2-}$, **b** DPPH, and **c** ·OH scavenging rate by MP and NCM@MP, respectively. **d** Fluorescence values of ROS level in BV2 microglia with different treatments. Indicators for oxidative stress, including **e** SOD, **f** MDA activity under different and neuroinflammation indicators **g** IL-1β, **h** TNF-α levels in LPS-triggered BV2 cells under different treatment conditions showed significant anti-oxidative stress response and anti-inflammatory of NCM@MP. **i** Calcium overloading degree tested by Fluo-4/AM Labeling which showed NCM@MP alleviated intracellular calcium levels. **j**–**l** Cell apoptosis representative images of H_2O_2-triggered SH-SY5Y cells treated by NCM@Mn_3O_4 and NCM@MP, which revealed neuroprotective function of NCM@MP in vitro. Data were mean ± SD (n = 3 per group). *$p < 0.05$, **$p < 0.01$, ***$p < 0.001$, ****$p < 0.0001$

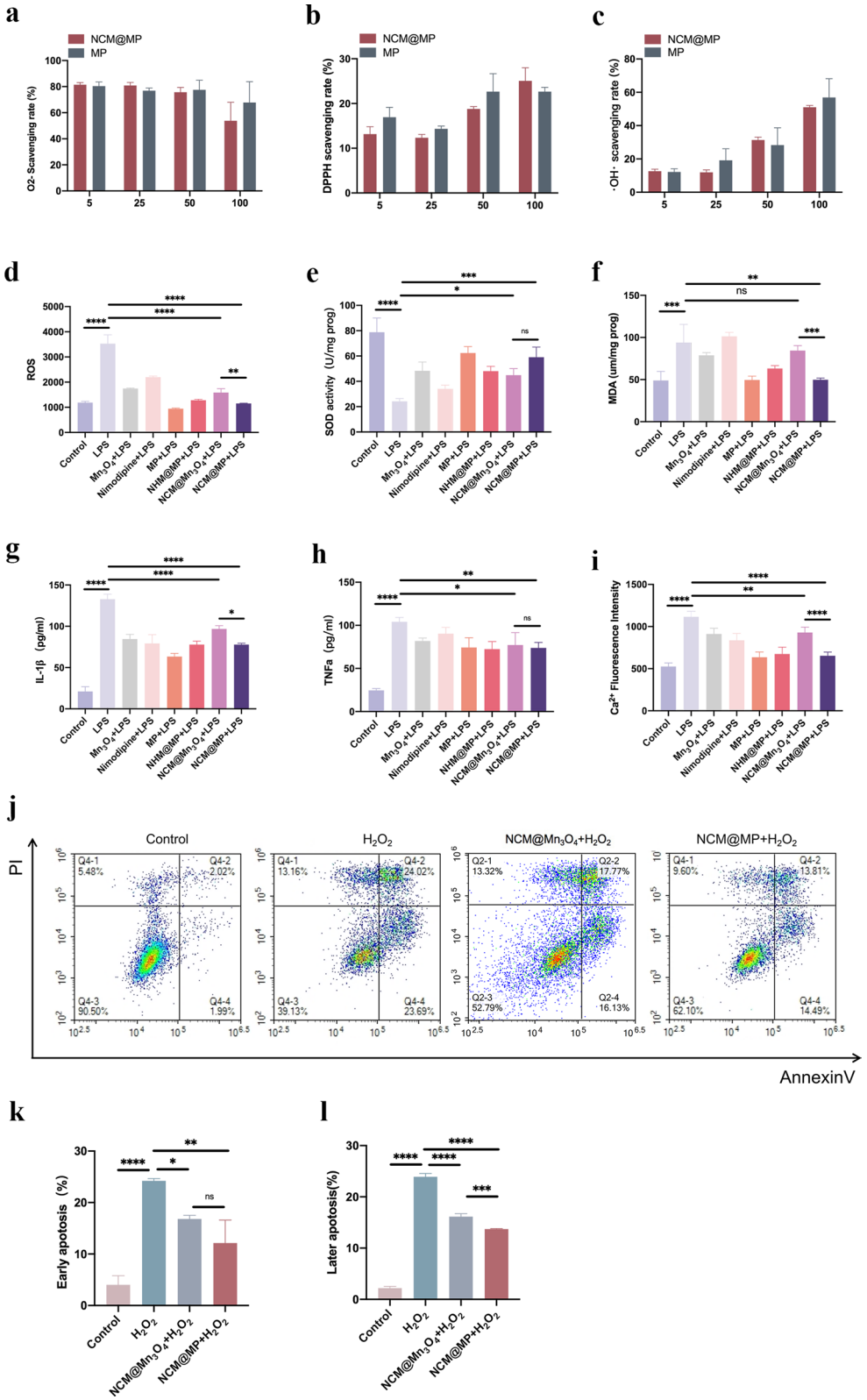

Fig. 2 (See legend on previous page.)

edema are associated with the poor prognosis of TBI [27]. Thus, we speculated that NCM@MP may significantly improve BBB integrity and relieve brain edema. The BBB integrity after TBI was evaluated by dynamic contrast-enhanced MRI (DCE-MRI) (Fig. 4c) and evans blue (EB) staining (Figure S10). Ktrans derived from DCE-MRI provides information on vascular permeability in vivo. Compared with the TBI group, the Ktrans values of the lesion were remarkably reduced in both NCM@Mn_3O_4 and NCM@MP groups at day-1 post-treatment. The mice treated with NCM@MP showed lower Ktrans values (Fig. 4d). Furthermore, the results of EB staining confirmed the findings of DCE-MRI, demonstrating that NCM@MP could protect the BBB efficiently (Figure S10). In addition, brain edema was assessed after 1-day post-treatment in these four groups. As expected, T2WI

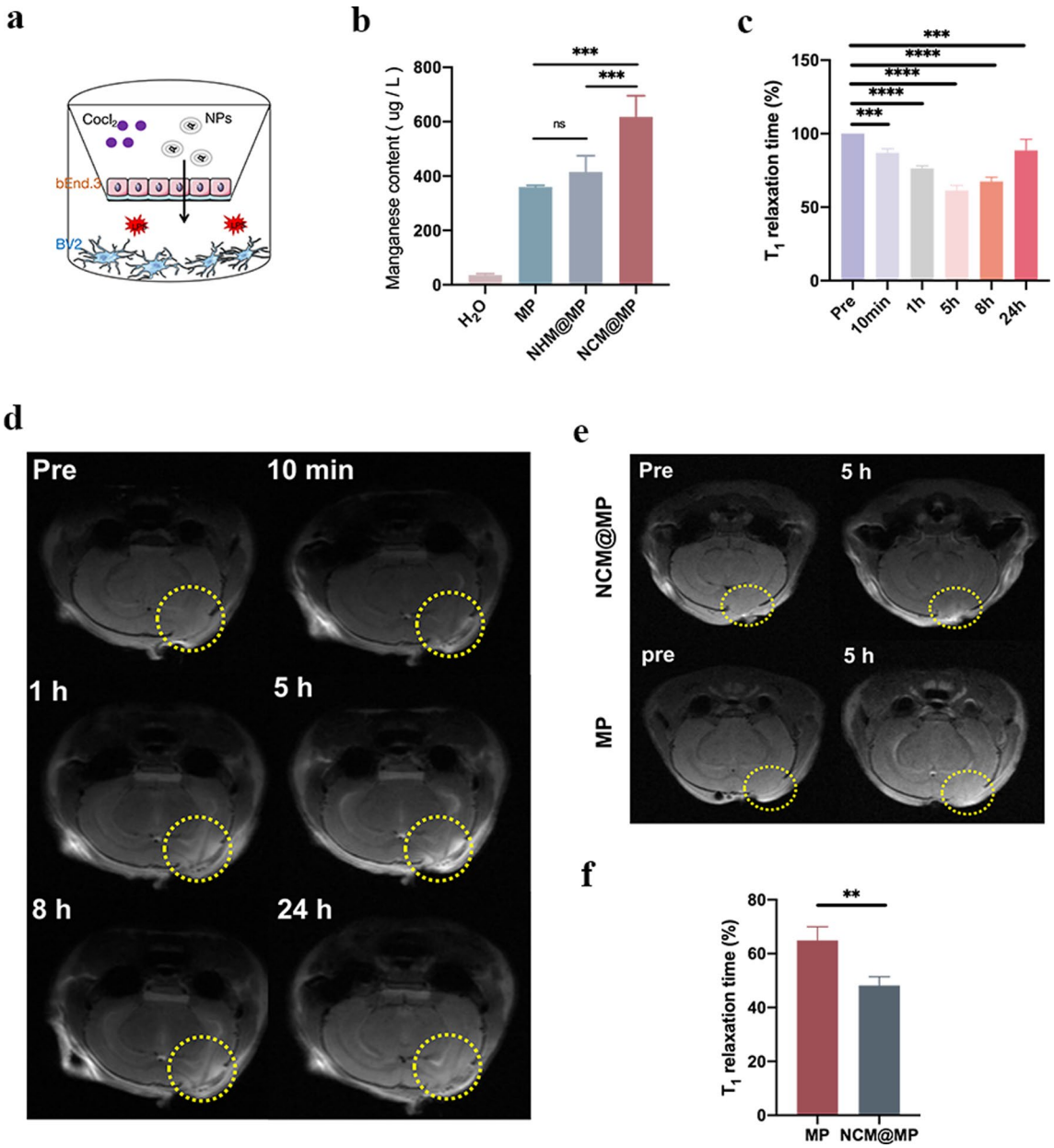

Fig. 3 **a**–**b** Targeting ability of NCM@MP in vitro evaluated by ICP-MS analysis. **c**–**d** In vivo T1WI and relaxation time of TBI lesion pre- and post-injection of NCM@MP at different time points. **e** The BBB-crossing ability of NCM@MP evaluated by T1 relaxation time. **f** T1 relaxation time were used to evaluate the ability of NCM@MP to target TBI. Data were mean ± SD (n = 5 per group). *$p < 0.05$, **$p < 0.01$, ***$p < 0.001$, ****$p < 0.0001$

also showed smaller areas of hyperintensity in both the NCM@Mn_3O_4 and NCM@MP groups, compared with the TBI group (Fig. 4e). Treatment with NCM@MP significantly decreased brain water content, compared with the TBI group (Fig. 4f). These results indicated that NCM@MP could relieve brain edema after brain injury. Next, we tested the effects of NCM@MP treatment on brain tissue loss after TBI. When imaged at a 4-week post-injection, both NCM@Mn_3O_4-treated and NCM@MP-treated mice had significantly reduced lesion volumes significantly (≈ 39%, 60%, respectively), compared with the TBI mice (Fig. 4g, h). Hematoxylin–eosin (HE) staining results showed that on 28 days post TBI, NCM@MP alleviated brain tissue loss (Fig. 4i). Morris water maze was performed to investigate the effect of NCM@MP on the learning and memory of the mice after TBI (Fig. 4j). Escape latency in training is a main index to reflect the learning ability. During the 5 training days, escape latency gradually reduced in all mice (Fig. 4k). In the testing, the memory ability of mice was assessed without the platform. The mice in the NCM@MP group found the hidden platform more quickly, compared with the TBI group, suggesting that NCM@MP could efficiently improve the learning ability of TBI mice. However, no significant difference was found between NCM@Mn_3O_4 and NCM@MP groups. (Fig. 4l). The platform entries during 60 s in NCM@MP-treated mice were more than TBI mice with significant differences (Fig. 4m). However, no significant differences were found between NCM@Mn_3O_4 and TBI groups in platform entries and latency to the first entry. The latency to first entry and platform entry times on 3_{rd} day post-TBI were more outstanding than 1_{st} day after treatment (Figure S11). These findings suggested that NCM@MP could improve the learning and memory abilities of TBI mice and was better for long-term cognitive impairment than in short. Compared with the untreated TBI groups, the modified neurological severity scores (mNSS) were lower in NCM@Mn_3O_4 and NCM@MP-treated TBI mice (Figure S12). In particular, NCM@MP-treated mice displayed the lowest mNSS scores compared with the other groups except the sham group, and improved injury scores compared with the TBI group on day 3 and 14 post-TBI, demonstrating that NCM@MP enhanced the neurological recovery of TBI mice to the greatest extent. Finally, the hanging wire grip test was performed to assess motor strength after NCM@MP treatment. As shown in Figure S13, NCM@MP-treated TBI mice showed increased maximum endurance compared to other groups, suggesting that the motor strength of TBI mice was enhanced after NCM@MP treatment. Taken together, these above-mentioned evidences suggested that NCM@MP could effectively alleviate brain injury.

Mechanisms underlying NCM@MP treatment in TBI mouse model

Neuroinflammatory response are contributing factors for TBI induced secondary injury. Pro-inflammatory cytokines such as IL-1β and TNF-α in the brain increased after TBI but were significantly reduced after NCM@Mn_3O_4 and NCM@MP treatment (Fig. 5a, b). In addition, we found that NCM@MP had better anti-inflammatory effects to IL-1β in the short term (1 day after TBI) than that in three days compared with NCM@Mn_3O_4 (Figure S14). These results suggested that NCM@MP had stronger short-term anti-inflammatory effects. To investigate mechanisms underlying NCM@MP treatment in TBI, we first tested the oxidative stress in the brain lesion. The level of SOD significantly decreased at 1-day post-injection in the TBI mice (Fig. 5c). Compared with the TBI group, levels of SOD were significantly elevated in NCM@MP groups. The treatment of NCM@MP also decreased the MDA level. Mice treated with NCM@MP exhibited lower levels of MDA than those treated with NCM@Mn_3O_4 (Fig. 5d). The overproduced ROS is known to induce inflammation after TBI [28]. The astrocytes and microglia were recruited enormously in the injured area [29]. The marker of reactive astrocytes, glial fibrillary acidic protein (GFAP) [30] and the marker of activated microglia, ionized calcium binding adapter molecule 1 (IBA1) [31], were used to investigate the anti-inflammatory effects of NCM@MP on TBI. On day 3 after TBI treatment, the mice in the TBI group showed significantly more activated astrocytes and microglia relative to the sham group, due to the acute immune response in the brain resulting from TBI (Fig. 5e). The

(See figure on next page.)

Fig. 4 **a**–**b** Injury area percentage was decreased by NCM@MP treatment on the 1st day after TBI using TTC staining. **c**–**d** Representative Ktrans map derived from DCE-MR imaging and quantitative analysis of the brain at 1-day post-treatment. **e**–**f** Representative T2WI and quantitative analysis of brain edema at 1-day post-treatment. **g**–**h** Representative T2WI and quantitative analysis of lesion volumes at 4 weeks post-injection. **i** Hematoxylin–eosin staining at 28-day post-treatment. These results showed NCM@MP improved BBB permeability and edema in TBI acute stage, and increased lesion defect recovery in chronic stage. **j**–**k** Swimming trajectories of mice and the time to find the platform in the training phase in four groups in the testing phase of water maze test. **l**–**m** Latency to first entry and platform entries on the test day. Results illustrated that the NCM@MP promoting the recovery of neuronal cognition and the spatial learning and memory abilities of TBI mice. Data were mean ± SD (n = 5 per group). *$p < 0.05$, **$p < 0.01$, ***$p < 0.001$, ****$p < 0.0001$

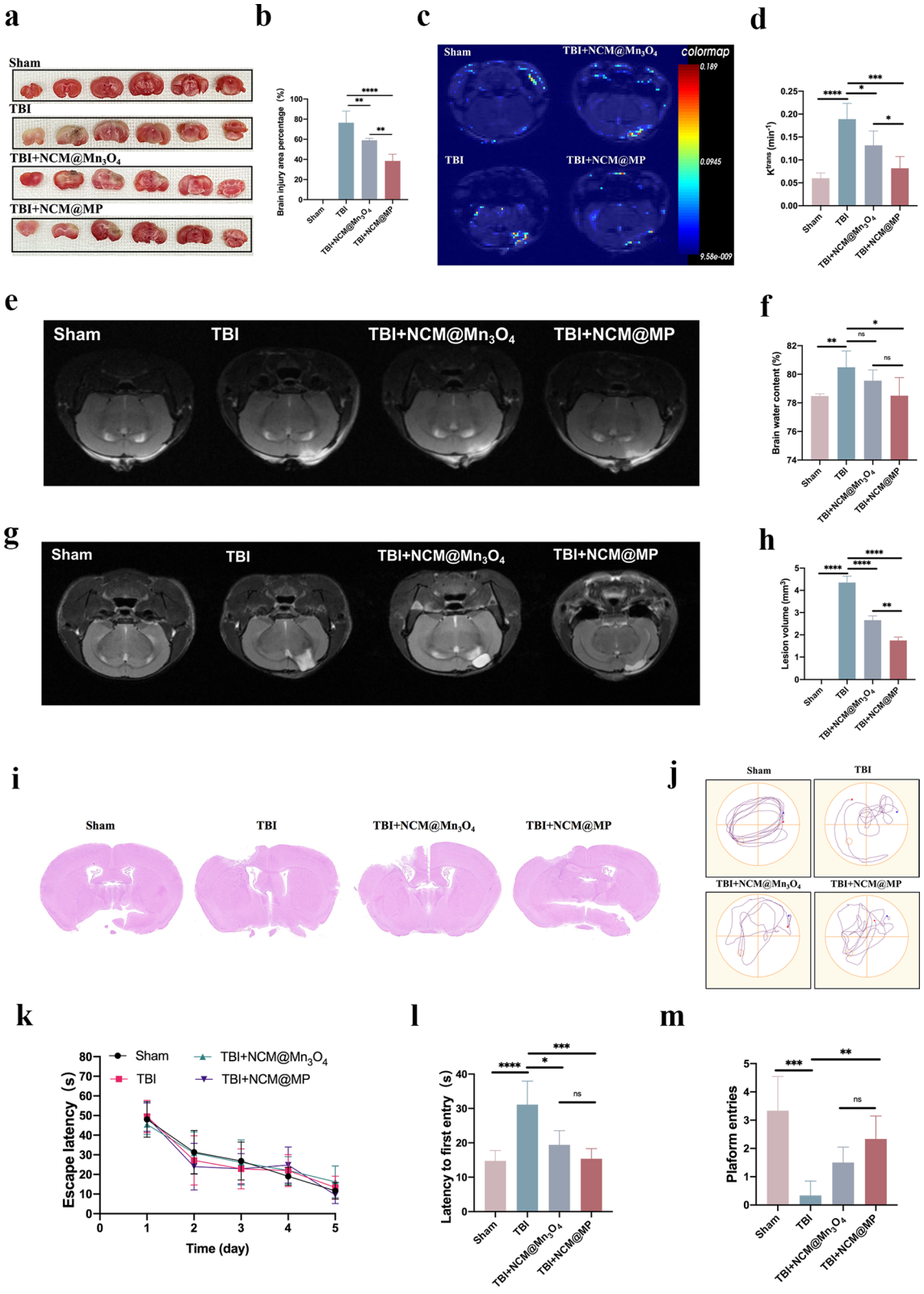

Fig. 4 (See legend on previous page.)

amount of activated astrocytes and microglia was obviously lower in the NCM@Mn_3O_4 and NCM@MP groups, relative to the TBI group. The mice treated with NCM@MP showed lower GFAP and IBA1 expressions than those treated with NCM@Mn_3O_4 (Fig. 5e). Polarization of microglial from M2 anti-inflammatory phenotype to M1 pro-inflammatory phenotype could result in neuroinflammation [32]. Therefore, the repolarization effect of NCM@MP on microglia was evaluated in vitro. As shown in Figure S15, samples treated with NCM@Mn_3O_4 and NCM@MP displayed a decrease of CD86/CD206 ratios by flow cytometry. This result indicated the robust capability of NCM@MP for repolarizing M1 into M2 macrophages. Neurogenesis marker, NeuN, plays a specific role in neuroprotective effect and has been reported to express in the developing and regenerating neurons [33]. At 4 weeks post-treatment, the NeuN expression significantly increased in the NCM@Mn_3O_4 and NCM@MP groups, relative to TBI group (Fig. 5f). In the NCM@MP group, the largest amount of NeuN expression was shown (Fig. 5f). SOX proteins are widely expressed in neuroepithelial precursor cells, mature neurons, and influence their identity, survival and development [34]. A similar trend was also observed in SOX expression (Fig. 5f). Taken together, these findings indicated that NCM@MP could alleviate oxidative stress, relieve neuroinflammation, and promote neuronal regeneration and functional recovery in the secondary injury of TBI. The mechanisms underlying these functions are relatively complex and remain unclear, but may be related to BV2 polarization phenotype [35]. TLR4/NF-kB pathway participated microglia/macrophages polarization and attenuated microglia inflammatory response [36]. PI3K-Akt is a well-known upstream regulator of the mTOR pathway, which has also been shown to affect macrophage polarization [37]. The impact of NCM@MP on TLR4/NF-κB and PI3K-Akt/mTOR is also unknown. Thus, we verified whether NCM@MP was involved in regulating the signaling TLR4/NF-κB and PI3K/mTOR pathway. As shown in Fig. 5g, NCM@MP down-regulated phosphorylation of NF-κB, PI3K/mTOR and TLR4 induced by H_2O_2 stimulation in BV2 microglia which could explain the anti-oxidative and anti-neuroinflammation function of NCM@MP.

The cytotoxicity and biosafety of NCM@MP

A perfect nano-drug should be low-toxicity for bio-applications. The cytotoxicity of NCM@MP was exerted on bEnd.3 cells, BV2 microglia and SH-SY5Y at a variety of concentrations (Fig. 6a–c), indicating excellent biocompatibility at the cellular level. Subsequently, the hemolysis rate of the NCM@MP (50 μg mL^{-1}) was 1.79%, indicating good hemocompatibility (Figure S9). Next, to investigate the cytotoxicity and biosafety of NCM@MP in vivo, serum biochemical detection and HE staining of the main organs were conducted. No significant injuries were found in biochemical indexes between the groups (Fig. 6d). In addition, no obvious injured evidence was shown on the main organs, which were harvested from mice that were injected with PBS or NCM@MP at day-14 post-treatment (Fig. 6e). These findings indicated the safety and suitability of NCM@MP for bio-applications in vivo. Noting that Mn is an essential element for the metabolism of organisms, Mn exists widely in all tissues of organisms, and nimodipine is approved by the Food and Drug Administration, which guarantees the biosafety of NCM@MP.

Conclusion

Reducing the detrimental effects of excessive calcium influx and scavenging damages caused by ROS are crucial for the clinical treatment of TBI. Therefore, it is necessary to enhance the antioxidative capacity when developing enzyme-mimetic nanomaterials for TBI therapy. In this particular investigation, we employed NCM@MP to mitigate ROS-induced damage in TBI. This innovative design not only overcame the limitations of MP but also offered additional advantages, including (i) The effective suppression of excessive calcium influx-mediated ROS generation and the accumulation of ROS produced by various substances can prevent ROS-induced secondary injuries in TBI. (ii) The reduction in the activation of astrocyte cells and microglia, as well as the decrease in inflammation levels, can be achieved. (iii) The improved protection provided by NCM@MP against TBI-induced

(See figure on next page.)

Fig. 5 **a**–**b** ELISA analysis of inflammatory factors IL-1β and TNF-α levels of the mice on day 1 post TBI with NCM@Mn_3O_4 or NCM@MP treatment confirmed the abilities on regulating inflammatory factors. **c**–**d** The brain SOD and MDA levels of the mice on day 1 after different treatment confirmed the anti-oxidative abilities of the NCM@MP on TBI mice. **e** Representative immunohistochemical images and quantification of GFAP in astrocytes and IBA1 in microglia from the injured tissues in TBI models at day 3 post-injection, which showed NCM@MP reduced glial cell activation in vivo. The scale bar denotes 50 μm. **f** Representative immunohistochemical images and quantification of SOX and NeuN in regenerated tissues at day 28 post-injection, which showed NCM@MP promoted neuronal regeneration. The scale bar denotes 20 μm for SOX and 50 μm for NeuN. **g** Representative western blot images and quantification of signaling pathway. Data were mean ± SD (n = 3 per group). *$p < 0.05$, **$p < 0.01$, ***$p < 0.001$, ****$p < 0.0001$

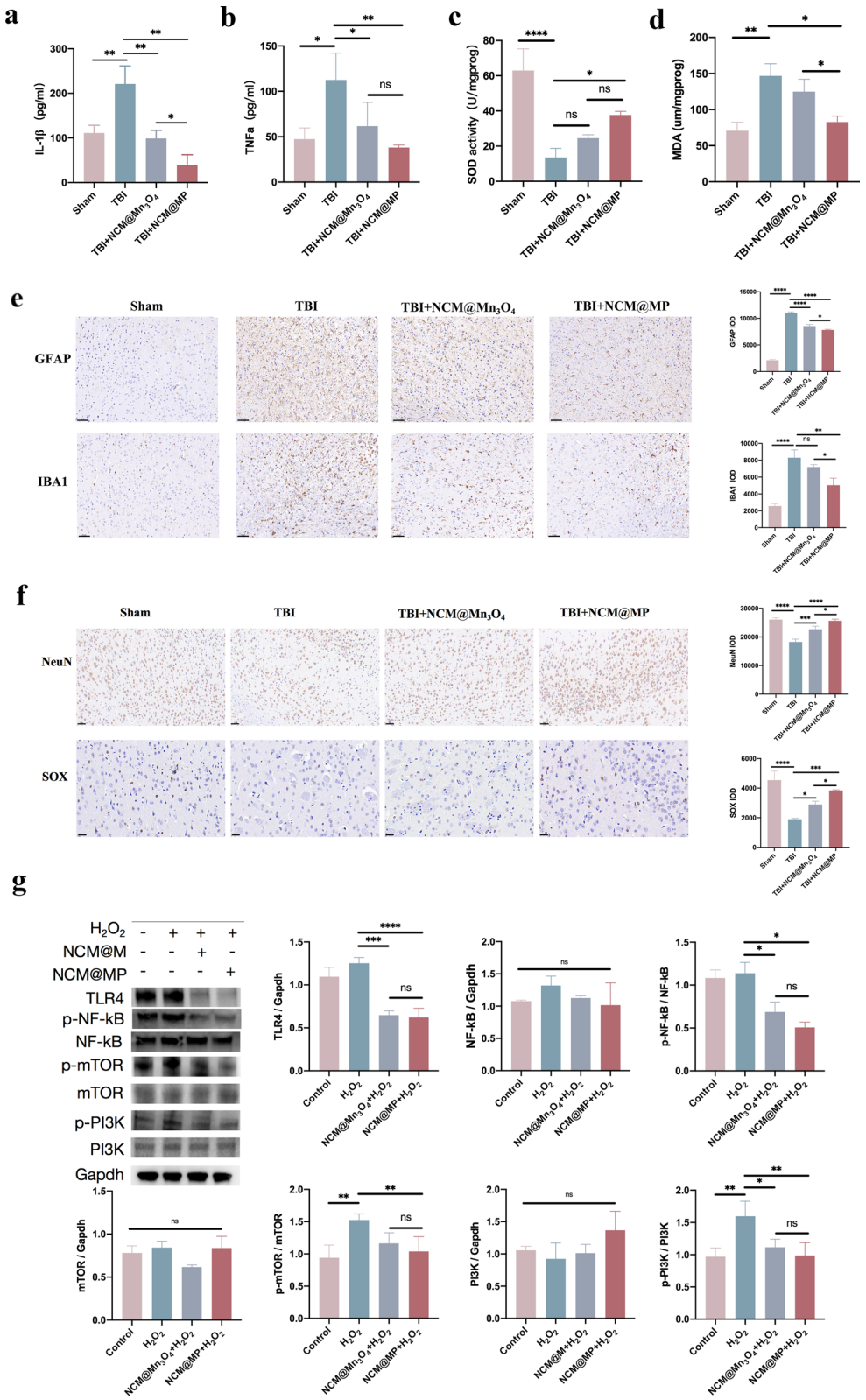

Fig. 5 (See legend on previous page.)

neuron apoptosis and the promotion of neuron regeneration can lead to the enhancement of memory and cognition recovery in mice after TBI. (iv) The release of manganese ions and nimodipine through the penetration of the BBB by neutrophil membranes, along with extended circulation times, enhanced accuracy in targeting injured tissues, and precise MRI. (v) NCM@MP is biocompatible. The outer layer of the nanoparticle is covered by the cell membrane components existing in the body, and the nanomaterial is small, which makes it safer to enter the blood circulation, and penetrate the BBB, then effectively target at the injured site. Cell membrane wrapping reduces the side effects caused by large doses of nimodipine alone. Together, this study not only demonstrates an improvement in the bioavailability of inflammatory tendency protein-stabilized MP but also sheds light on the underlying mechanisms of NCM@MP against TBI by scavenging ROS. The better therapeutic effects and biological safety of NCM@MP have proven its therapeutic potential on TBI and ROS-related diseases.

Experimental section

Synthesis of Mn_3O_4 NPs

$MnCl_2{\cdot}4H_2O$ (0.99 g) and sodium oleate (4.56 g) were dissolved in a mixture of double distilled water (ddH_2O, 20 mL) and anhydrous ethanol (10 mL). When the solid was completely dissolved, the mixed solution was heated (70 °C, 4 h) then washed 3 times using ddH_2O and dissolved in n-hexane for getting waxy-like manganese oleate. Manganese oleate (0.62 g, 1 mmol) was dissolved with oleic acid (158.7 μL,0.5 mmol) in 1-octadecene (12 mL) at room temperature. The mixture was degassed (vacuum, 20 min) and backfilled with nitrogen at room temperature to remove oxygen. To remove any low volatile substances, the solution was heated (90 °C, 30 min). After the reaction, the reaction solution was heated (300 °C, 20 min) and cooled to room temperature. Isopropyl alcohol (30 mL) was added to mix precipitation nanoparticles, and the precipitation was collected by centrifugation and washed with ethanol 3 times. All the precipitate was dissolved in 12 mL 1-octadecene at room temperature, followed by the addition of oleamine (660.7 μL, 2.05 mmol), and then the reaction solution was heated in the air (150 °C, 1 h). After the reaction, the obtained solution was cooled to room temperature, and the precipitation was centrifugated by isopropyl alcohol and washed with ethanol 3 times as previously. After washed, the precipitation was redissolved in n-hexane and stored in a refrigerator at 4 °C.

Cell cultures

HL-60 cells and BV2 microglia were donated by the Department of Gastroenterology of Daping Hospital (Army Medical University, Chongqing, China). bEnd.3 cells and SH-SY5Y cell lines were purchased from the Procell Life Science & Technology Co., Ltd. (Wuhan, China). bEnd.3, BV2 microglia and SH-SY5Y cell were cultured in DMEM/F12 (Gibco, Thermo Fisher Scientific, USA) containing 10% fetal bovine serum (FBS; Gibco, USA) and 1% penicillin/streptomycin (Sigma, USA). HL-60 cells were cultured in RPMI 1640 medium (Gibco, USA) supplemented with 20% FBS and 1% penicillin–streptomycin. All the cell lines were cultured in a humidified incubator at 37 °C and under 5% CO_2 atmosphere.

Cell membrane derivation

NHM was harvested following a previously published protocol [38]. Briefly, HL-60 cells were collected and washed with 1 × PBS three times (centrifugation at 1000 rpm). Cells were then suspended in hypotonic lysing buffer containing 30 mM Tris–HCl (pH 7.5), 225 mM d-mannitol, 75 mM sucrose, 0.2 mM EGTA (all reagents from Sangon Biotech, Shanghai, China) and a protease and phosphatase inhibitor cocktail (Beyotime, Shanghai, China). Subsequently, cells were disrupted with an ultrasonic homogenizer (JY92-IIN, SCIENTZ). The homogenized solution was centrifuged at 20,000 g (4 °C, 25 min). The pellet was discarded and the supernatant was centrifuged again at 100,000 g (4 °C, 35 min). Following the centrifugation, membranes were collected as the pellet and washed twice with 0.2 mM EDTA in double distilled water. Membrane content was quantified using a Bicinchoninic Acid (BCA) kit (Beyotime, Shanghai, China). Membranes were suspended with 0.2 mM EDTA to a protein concentration of 2 mg mL^{-1} and stored at − 80 °C for subsequent studies. HL-60 cells were differentiated to neutrophil-like cells in RPMI 1640 medium supplemented with DMSO at 1.3% (v./v.) for 5 days and NCM was collected as previously.

NCM@MP preparation

The resultant Mn_3O_4 NPs were mixed with NCM at a 1:2 (w/w) ratio of Mn_3O_4-to-membrane protein to produce NCM@Mn_3O_4. The mixture was extruded through polycarbonate membranes with a pore size of 100 nm. Free ammonium sulfate was removed by overnight dialysis in 10% sucrose solution with PBS. Then, nimodipine was mixed with the NCM@Mn_3O_4 at a 1:10 ratio of drug-to-Mn_3O_4 (w/w) for transmembrane ammonium sulfate gradient-driven loading to produce NCM@MP [13, 39].

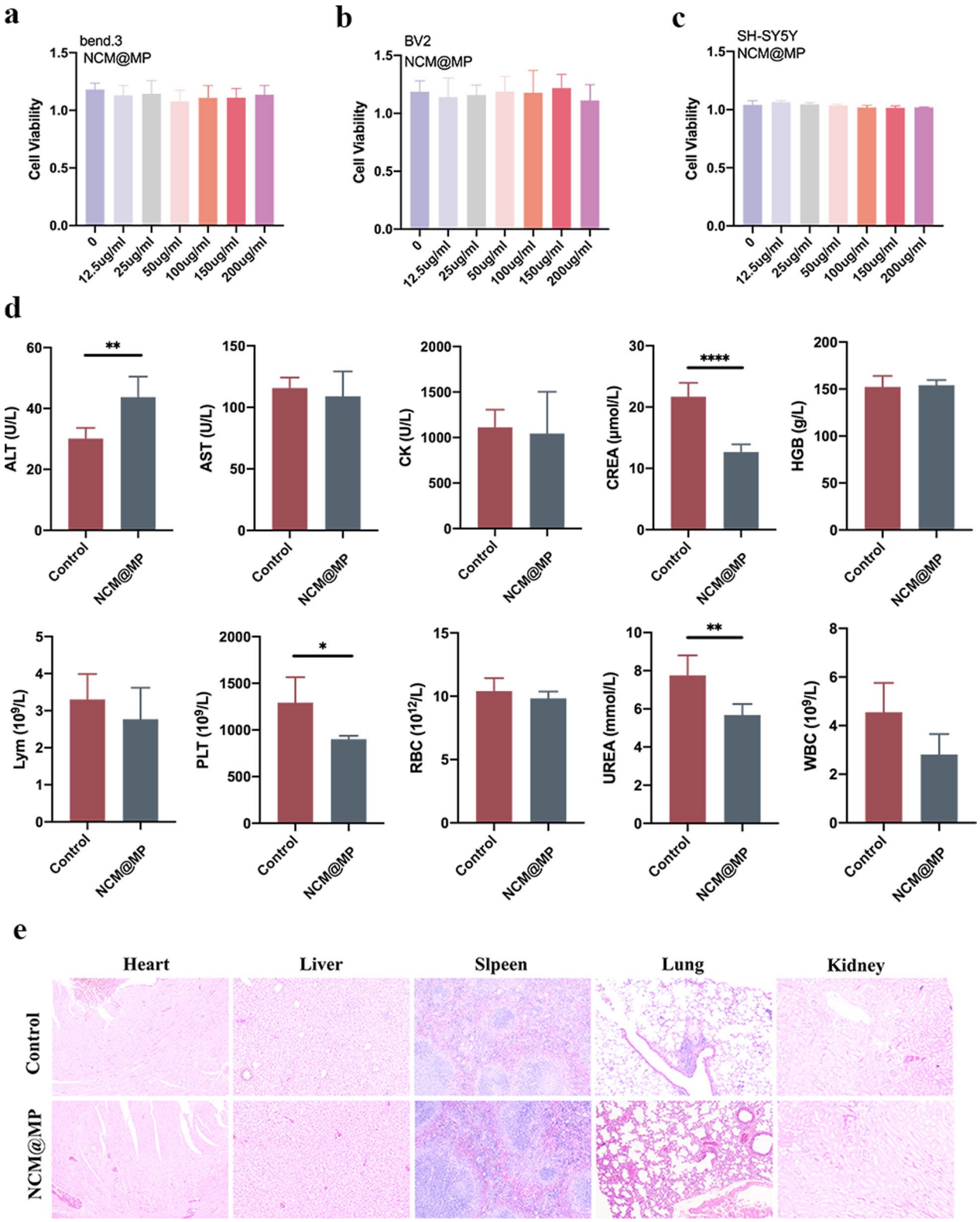

Fig. 6 **a**–**c** The cell viability of bEnd.3, BV2 and SH-SY5Y treated with a variety of concentrations of NCM@MP and there were no significant vitality changes. **d**–**e** Serum biochemical indexes and HE staining of the main organs of the mice at 14 days post-treatment. These results showed great biocompatibility of NCM@MP. Data were mean ± SD (n = 5 per group). *$p < 0.05$, **$p < 0.01$, ***$p < 0.001$, ****$p < 0.0001$

The dispersion was dialyzed in 250 volumes of PBS to remove the ammonium sulfate outside of membrane.

Cytotoxicity evaluation of NCM@MP

Cell viability was measured using the Cell Counting Kit-8 (CCK-8) assay (Beyotime, Shanghai, China). 90 μL DMEM/F-12 containing 5×10^3 bEnd.3 cells, 5×10^3 BV2 microglia and 8×10^3 SH-SY5Y cells were seeded in 96-well plates per well separately. To determine dose-dependence cytotoxicity, cells were treated with various doses of Mn_3O_4 (12.5, 25, 50, 100, 150, and 200 μg mL^{-1}), nimodipine (12.5, 25, 50, 100, 150, and 200 μg mL^{-1}) and NCM@MP (12.5, 25, 50, 100, 150, and 200 μg mL^{-1}) for 24 h. After treatment, 10 μL CCK-8 (Beyotime, Shanghai, China) were added to each well (37 °C, 2 h). Then microplate reader (BioTek Instruments, CA, USA) was used to determine sample absorbance at 450 nm.

Western blot analysis

The total protein levels were detected by BCA protein assay kits (Beyotime, Shanghai, China). In brief, the supernatant of cells and mice brain tissues was lysed with radio immuno-precipitation assay (RIPA) buffer containing phenylmethyl sulfonyl fluoride (PMSF) and centrifuged at 12, 000 rpm/min for 10 min. Protein concentrations were measured using BCA kits. Protein mixtures (20 μL per lane) were separated using sodium dodecyl sulfate–polyacrylamide gel electrophoresis (SDS-PAGE) and transferred onto polyvinylidene difluoride (PVDF) membranes (0.45 μm, Millipore). Membranes were blocked with 5% nonfat dry milk for 2 h at room temperature. Determining the concentrations of protein, the cell extraction incubated with primary antibody was performed overnight at 4 °C. The following primary antibodies were used: Integrin β1 (Abcam, 1:1000, USA), CXCR4 (Abcam, 1:100, USA), Mac-1 (CST, 1:1000, USA), mTOR (CST, 1:1000, USA), p-mTOR (CST, 1:1000, USA), PI3K (CST, 1:1000, USA), p-PI3K (CST, 1:1000, USA), TLR-4 (CST, 1:1000, USA), NF-kB (CST, 1:1000, USA), p-NF-kB (CST, 1:1000, USA), GAPDH (CST, 1:1000, USA), Na–K ATP (CST, 1:1000, USA). The next day, the membranes were washed 3 times for 5 min each with TBST and then incubated with HRP-conjugated secondary antibody (1:10,000 dilution) for 2 h at room temperature. Western Blot signals were detected by chemiluminescence with Chemidoc software (Bio-Rad, Munich, Germany).

Detection of free radicals scavenging in vitro

The measurement of free radicals scavenging by nanomaterials was assessed via relevant assay kits (Solarbio, Beijing, China) which detect the level of 2,2-diphenyl-1-picrylhydrazyl (DPPH), hydroxyl radicals (·OH) and superoxide radicals ($\cdot O^{2-}$), respectively, according to the manuals.

Enzymatic activity of SOD and MDA

For detection of the oxidative stress level changes induced by LPS in BV2 microglia treated with NCM@MP, total SOD and MDA assay kits (Beyotime, Shanghai, China) were used to evaluate the activity of enzymes. Supernatants from cells after treatment were collected to be detected according to the manual of the kit. Equivalent components were added respectively.

In mice, brains from mice in four groups were harvested at 1-day post-injection. SOD and MDA sample preparation solution and brain tissues were homogenized at 4 °C. The samples were centrifuged at 12,000 g at 4 °C for 5 min and the supernatant was taken to be detected according to the manual.

Intracellular ROS scavenging

The equal BV2 cells were inoculated in 6-well plates at 37 °C in 5% CO_2 for 24 h. Then, 50 μg mL^{-1} NCM@MP was added 30 min previously. Equivalent components were added respectively.

Subsequently, 1 μg mL^{-1} LPS (Sigma Aldrich, St. Louis, MO) was added and co-cultured for 24 h. Then, DCFH-DA was diluted with serum-free DMEM/F12 medium at 1:1000 to a final concentration of 10 μM. The cells were collected and suspended in diluted DCFH-DA and then incubated in a cell incubator (37 °C, 30 min). Mix upside down every 5 min to allow full contact between the probe and the cell. Cells were washed three times with serum-free cell culture medium to adequately remove extra DCFH-DA that did not enter the cells. The fluorescence intensity of the cells was quantified by a luciferase microplate reader (Spectra Max i3x, Molecular Devices, USA) with 488 excitation wavelength and 525 nm emission wavelength.

Inflammatory cytokine measurement

At the cellular level, LPS (1 μg mL^{-1}), NCM@MP (50 μg mL^{-1}) were added and co-cultured with cells for 24 h. Equivalent components were added respectively. Brains form four groups after treatment were sacrificed at 1-day and 3-day post TBI. ELISA kits (Solarbio, Beijing, China) were used to detect the levels of TNF-α and IL-1β in supernatants according to manuals.

Calcium labeling by Fluo4/AM

Fluo-4/AM, an acetyl methyl ester derivative of Fluo-4, is a fluorescent dye that can penetrate cell membranes and can be shared by the esterase inside the cell to form Fluo-4, binding to calcium ions, and after binding calcium ions, it can produce strong fluorescence. Fluo-4 AM kits

(Beyotime, Shanghai, China) were used to detect the levels of calcium according to manuals.

BBB in vitro model and cellular uptake of NCM@MP

The Transwell BBB model was established as previously reported [40]. The bEnd.3 cells (5×10^4 cells per well) were seeded in the Transwell (0.4 μm pore size) and 1×10^4 BV2 incubated on the lower chamber, co-culturing for 3 days. To simulate BBB leakage and neuroinflammation, the upper chamber was treated with 200 μM $CoCl_2$ (Sigma Aldrich, St. Louis, MO) and 1 μg mL^{-1} LPS 24 h was for the lower. The medium containing NCM@MP (50 μg mL^{-1}), equivalent components were added to the apical chamber for 6 h respectively. The component of manganese in the basal chamber of three groups was measured by ICP-MS (Agilent ICPMS7800, Agilent, CA, USA). For cellular uptake of NCM@MP BV2 cells were incubated with NCM@MP (50 μg mL^{-1}) for 24 h, then washed with PBS for 3 times and observed by TEM.

Microglial staining and flow cytometry

Microglias were cultured in DMEM/F12 containing 10% FBS, 1% penicillin–streptomycin, and NCM@Mn_3O_4 or NCM@MP (50 μg mL^{-1}) culture media for 24 h. To induce them into M1-like microglia, cells were stimulated with H_2O_2 (1 μM) for 24 h, respectively. Subsequently, all types of cells were collected and double stained CD86 (1:100, GL1, eBioscience, San Diego, CA, USA), and CD206 (1:100, MR6F3, eBioscience, San Diego, CA, USA) for flow cytometry (NovoCyte Flow Cytometer, NovoCyte D2060R, USA).

Cell apoptosis assay using annexin V-FITC/PI double staining

The effect of NCM@MP on the death of SH-S5SY cells was explored by flow cytometry. Briefly, cells were seeded onto 6-well cell culture plates at a density of 1×10^6 cells per well. Following H_2O_2 stimulation (1 μM, 24 h) with NCM@Mn_3O_4 or NCM@MP (50 μg mL^{-1}) treatment, cells were collected and washed with cold PBS and were resuspended in 100 μL reaction buffer containing 5 μL Annexin V–FITC and 10 μL PI (Biolegend, San Diego, CA, USA). Cell solutions were then incubated for 15 min at room temperature in the dark. Finally, 400 μL of the binding buffer was added to each sample and then the fluorescence was quantified by flow cytometry. Positive staining for Annexin V is indicative of apoptosis and PI staining differentiates early and late apoptotic phases. Cells with positive Annexin V and negative PI are in the early apoptotic phase, while cells that are positive for both Annexin V and PI underwent late apoptosis.

TBI animal models

All animal procedures were approved by Laboratory Animal Welfare and Ethics Committee of Third Military Medical University, Chongqing, China (AMUWEC20211645). Experimental C57BL/6 mice (6–8 weeks, male) were purchased from Beijing Vital River Laboratory Animal Technology Co., Ltd. (Beijing, China). Mice in the sham group were conducted only with craniotomy. The TBI model was established by CCI as previously reported [41]. Mice in TBI + NCM@Mn_3O_4 and TBI + NCM@MP groups, NCM@Mn_3O_4 or NCM@MP (1.59 mg kg^{-1} body weight) were administered via tail vein respectively 6 h after TBI induction.

Half-life time detection of NCM@MP

NCM@MP (1.59 mg kg^{-1} body weight) was injected into mice through tail vein 24 h post TBI, mice were anesthetized and blood was quickly collected at several time points (30 min, 1 h, 2 h, 4 h, 8 h, 12 h, 24 h) and serum were centrifuged. The supernatant was extracted for Mn detection by ICP-MS.

Morris water maze

Morris water maze was administered to assess spatial learning and memory. The water maze included 4 quadrants and one of the four quadrants had a movable platform at a distance of 1 cm below the water surface. After the training phases which lasted 4 days, each mouse was randomly released from one of four quadrants and faced the pool wall at the same time. Once the mice found the platform by themself within 120 s, they could stay for 10 s. If the animal failed to reach the platform in 2 min, it would be guided toward the hidden platform and stayed for 10 s. All mice were initially tested in a probe trial on the 5th day to ensure effective training. On post-TBI days 1 and 3, the platform was removed and the mouse was allowed to search the quadrant for the platform for 2 min. The latency and crossing times of the platform were recorded by the behavioral software (Version 2.1 Beijing Sunny Instruments Co. Ltd, Mouse Track).

mNSS score and motor function test

As previously reported [5], mNSS score were conducted on the 1, 3, 7, 14, 28 d after TBI, which include movement (muscle state and abnormal movement), sensation (vision, touch, and proprioception), reflex response, and balance tests. Scores range from 0 (normal) to 18 (maximum defect). Motor deficit measurements were conducted on the day-28 after TBI by Hanging Wire Grip Test. The mice grabbed the wire with their forearms and the time was recorded from start to fall to evaluate motor function.

In vivo MRI

MRI scanning was accomplished using a 7.0 T MR scanner (Bio-Spec, Bruker, Karlsruhe, Germany). The parameters of the scanning sequences, including T1 RARE, Turbo RARE-T2 and DCE-MRI, were performed as previously reported [42]. For in vivo MRI, the TBI mice were scanned before and 10 min, 1 h, 5 h, 8 h, 24 h after NCM@MP injection (1.59 mg kg^{-1} body weight) with T1 RARE, and Turbo RARE-T2. Lesion volume were calculated by ITK-SNAP 3.8.0 software (available at www.itksnap.org). In addition, to evaluate the target capability of NCM@MP relative to MP, TBI mice were performed T1 RARE and Turbo RARE-T2 at 5 h post injection of NCM@MP or MP. DCE-MRI was performed on the day 1 post injection for detecting BBB permeability in vivo.

BBB integrity assay

EB (Solarbio, Beijing, China) was used to detect the BBB integrity after TBI [41]. After intervention, each mouse was injected 0.5% EB at a dose of 2.5 mL per kg body weight through the tail vein. 1 h later, a lethal dose of sodium pentobarbital (100 mg kg^{-1}, i.p.) was administered, and the thoracic cavity was exposed. The animals were perfused transcardially through the left ventricle with physiological saline solution which continued for about 15 min. Following perfusion, mice were harvested to gain brains and weighed. Then using 1 mL PBS mixed with dimethylformamide (1:1) to homogenate each sample for 2 min and 1 mL of 60% trichloroacetic acid was added at 4 °C to precipitate proteins for 30 min. Then centrifuged at 18,000 g at 4 °C for 10 min. 200 μL supernatants were put into microplate containers, and the concentration of EB dye in the supernatant is analyzed at a wavelength of 620 nm spectrophotometrically by using a microplate reader (BioTek Instruments, CA, USA). The tissue content of Evans blue was quantified from a linear standard curve derived from the dye and expressed in μg per mg of brain tissues.

TTC staining

As previously reported [26], Infarction volume was measured using TTC staining on the 1st day after TBI. An intracardiac perfusion of saline was given to the animals under deep anesthesia. The brain tissue was then removed, immersed in cold saline (−20 °C, 20 min) and then sliced into 1.0 mm sections. The brain slices were incubated in 2% TTC (37 °C, 30 min) and then transferred to 4% formaldehyde solution for fixation. Negative TTC stains indicating the injury area. Percentages were measured in each slice and summed using Image J (Version 1.53, USA).

Brain water content

NCM@MP (1.59 mg kg^{-1} body weight) was injected after TBI, and cerebral edema was assessed 1 day later. In brief, mice were sacrificed and their brain tissues were removed without perfusion. The wet weights were measured on a microbalance. Dry weights were gained after heating the specimens (72 °C, 72 h). The brain water content was calculated by using the following formula: (wet weight-dry weight) /wet weight × 100%.

Mouse tissue immunohistochemistry and HE staining

Brain tissues from mice in these four groups were sectioned. HE staining and immunochemistry were performed as previously reported [24]. The sections with incubated with primary antibodies, including anti-mouse IBA1, anti-mouse GFAP (Abcam, USA), anti-mouse NeuN and anti-mouse SOX (CST, USA) followed by secondary antibodies, including biotinylated goat anti-rabbit and anti-mouse IgG (Beyotime, Shanghai, China). Images were acquired by Olympus BX43 microscope (Olympus America, Center Valley, PA, USA). Integrated optical density was used to evaluate the protein immunoreactivity by Image-Pro Plus 6.0 (Media Cybernetics, Rockville, MD, USA).

Hemolysis analysis of NCM@MP

Red blood cells (RBCs) were used to measure hemolysis. The RBCs were separated from mice blood samples and mixed with saline for later use. Subsequently, 100 μL RBCs were added into 1 mL NCM@MP (25, 50, 75 and 100 μg mL^{-1}) and cocultured (37 °C, 3 h). The saline was used as the negative control and deionized water was used as positive control. All the above samples were centrifugated and measured the absorbance at 540 nm. The formula of hemolysis percentage was as follows: Hemolysis (%) = (As − An)/(Ap − An) × 100%. Among them, As, An, and Ap were the absorbance of supernatant after incubating NCM@MP, saline, and deionized water with the RBCs suspension, respectively.

Serum biochemical analysis

NCM@MP (1.59 mg kg^{-1} body weight) was intravenously administrated into healthy C57BL/6 mice. The blood samples of mice were collected for the analysis of various blood biochemicals through a Biochemical Autoanalyzer (Type 7170, Hitachi, Japan) after 14 days. Simultaneously, tissues including heart, liver, spleen, lung, and kidney were taken to paraffin embedding and sectioned for HE staining.

Statistical analysis

All data are represented as mean ± standard deviation (SD) with at least 3 individual experiments. Statistical analysis was performed using unpaired t-test or one-way analysis of variance (ANOVA), and statistical significance (*P* value) was calculated in GraphPad Prism 8.0 (Boston, MA, USA). Results were considered significant at the 95% confidence level.

Supplementary Information

The online version contains supplementary material available at https://doi.org/10.1186/s12951-024-02753-5.

Supplementary material 1.

Acknowledgements

This work was supported by grants from Chongqing Science and Health Joint Medical Research Project-Young and Middle-aged High-level Talent Project (2023GDRC002 to X.C.), Science and Technology Innovation Ability Enhancement Project of Army Medical University (2022XJS29 to X.C.), Natural Science Foundation of Chongqing (cstc2019jcyj-msxmX0123 to X.C.), and Chongqing Clinical Research Centre of Imaging and Nuclear Medicine (CSTC2015YFPT-gcjsyjzx0175 to X.C.).

Author contributions

Conceptualization: H.Q. Li, D. Sun, K.J. Liu and X. Chen; data curation: H.Q. Li and D. Sun; formal analysis: H.Q. Li, D. Sun and X. Chen; funding acquisition: X. Chen; investigation: H.Q. Li, D. Sun and C.Q. Lv; methodology: H.Q. Li, D. Sun and C.Q. Lv; project administration: K.J. Liu and X. Chen; resources: Z.H. Zhao, J.Q. Fang, M.Y. Li, W.C. Zhou, N. Li, Y. Guo, Z.L. Cao, K.J. Liu and X. Chen; software: H.Q. Li, D. Sun, Y. Guo, Z.L. Cao and X. Chen; supervision: K.J. Liu and X. Chen; validation: H.Q. Li and D. Sun; visualization: H.Q. Li and D. Sun; writing—original draft: H.Q. Li and D. Sun; writing—review & editing: H.Q. Li and X. Chen.

Funding

This work was supported by grants from Chongqing Science and Health Joint Medical Research Project-Young and Middle-aged High-level Talent Project (2023GDRC002 to X.C.), Science and Technology Innovation Ability Enhancement Project of Army Medical University (2022XJS29 to X.C.), Natural Science Foundation of Chongqing (cstc2019jcyj-msxmX0123 to X.C.), and Chongqing Clinical Research Centre of Imaging and Nuclear Medicine (CSTC2015YFPT-gcjsyjzx0175 to X.C.).

Availability of data and materials

All data and materials are showed in the paper and further inquiries can be directed to the corresponding author.

Declarations

Ethics approval and consent to participate

All animal procedures were approved by Laboratory Animal Welfare and Ethics Committee of Third Military Medical University, Chongqing, China (AMUWEC20211645).

Consent for publication

All authors agreed to publish this manuscript.

Competing interests

The authors declare that they have no competing interests.

Author details

[1]Department of Nuclear Medicine, Daping Hospital, Army Medical University, Chongqing 400042, China. [2]College of Basic Medicine, Chongqing Medical University, Chongqing 400016, China. [3]Department of Ultrasound, Daping Hospital, Army Medical University, Chongqing 400042, China. [4]Department of Gastroenterology, Daping Hospital, Army Medical University, Chongqing 400042, China. [5]Department of Radiology, Daping Hospital, Army Medical University, Chongqing 400042, China.

Received: 6 November 2023 Accepted: 2 August 2024
Published online: 12 August 2024

References

1. Kalra S, Malik R, Singh G, Bhatia S, Al-Harrasi A, Mohan S, Albratty M, Albarrati A, Tambuwala MM. Pathogenesis and management of traumatic brain injury (TBI): role of neuroinflammation and anti-inflammatory drugs. Inflammopharmacology. 2022;30:1153–66.
2. Werner C, Engelhard K. Pathophysiology of traumatic brain injury. Br J Anaesth. 2007;99:4–9.
3. Tehse J, Taghibiglou C. The overlooked aspect of excitotoxicity: glutamate-independent excitotoxicity in traumatic brain injuries. Eur J Neurosci. 2019;49:1157–70.
4. Feno S, Butera G, Reane DV, Rizzuto R, Raffaello A. Crosstalk between calcium and ROS in pathophysiological conditions. Oxid Med Cell Longev. 2019. https://doi.org/10.1155/2019/9324018.
5. Han Z, Han Y, Huang X, Ma H, Zhang X, Song J, Dong J, Li S, Yu R, Liu H. A novel targeted nanoparticle for traumatic brain injury treatment: combined effect of ROS depletion and calcium overload inhibition. Adv Healthc Mater. 2022;11:e2102256.
6. Carlson AP, Hänggi D, Macdonald RL, Shuttleworth CW. Nimodipine reappraised: an old drug with a future. Curr Neuropharmac. 2020;18:65–82.
7. Wu J, Wang X, Wang Q, Lou Z, Li S, Zhu Y, Qin L, Wei H. Nanomaterials with enzyme-like characteristics (nanozymes): next-generation artificial enzymes (II). Chem Soc Rev. 2019;48:1004–76.
8. Yao J, Cheng Y, Zhou M, Zhao S, Lin S, Wang X, Wu J, Li S, Wei H. ROS scavenging Mn(3)O(4) nanozymes for in vivo anti-inflammation. Chem Sci. 2018;9:2927–33.
9. Li K, Li P, Wang Y, Han S. Manganese-based targeted nanoparticles for postoperative gastric cancer monitoring via magnetic resonance imaging. Front Oncol. 2020;10:601538.
10. Gronloh MLB, Arts JJG, van Buul JD. Neutrophil transendothelial migration hotspots - mechanisms and implications. J Cell Sci. 2021. https://doi.org/10.1242/jcs.255653.
11. Phillipson M, Heit B, Colarusso P, Liu L, Ballantyne CM, Kubes P. Intraluminal crawling of neutrophils to emigration sites: a molecularly distinct process from adhesion in the recruitment cascade. J Exp Med. 2006;203:2569–75.
12. Yu X, Wang D, Wang X, Sun S, Zhang Y, Wang S, Miao R, Xu X, Qu X. CXCL12/CXCR4 promotes inflammation-driven colorectal cancer progression through activation of RhoA signaling by sponging miR-133a-3p. J Exp Clin Cancer Res. 2019;38:32.
13. Feng L, Dou C, Xia Y, Li B, Zhao M, Yu P, Zheng Y, El-Toni AM, Atta NF, Galal A, et al. Neutrophil-like cell-membrane-coated nanozyme therapy for ischemic brain damage and long-term neurological functional recovery. ACS Nano. 2021;15:2263–80.
14. Bonetta R. Potential therapeutic applications of MnSODs and SOD-mimetics. Chemistry. 2018;24:5032–41.
15. Tsikas D. Assessment of lipid peroxidation by measuring malondialdehyde (MDA) and relatives in biological samples: analytical and biological challenges. Anal Biochem. 2017;524:13–30.
16. Nantapong N, Murata R, Trakulnaleamsai S, Kataoka N, Yakushi T, Matsushita K. The effect of reactive oxygen species (ROS) and ROS-scavenging enzymes, superoxide dismutase and catalase, on the thermotolerant ability of Corynebacterium glutamicum. Appl Microbiol Biotechnol. 2019;103:5355–66.
17. Li H, Liu F, Jiang W, Wang K, Cao X, Zou J, Zhou Y, Li Z, Liu S, Cui X, Zhang X. TREM2 ameliorates lipopolysaccharide-induced oxidative stress response and neuroinflammation by promoting Sirtuin3 in BV2 cells. Neurotox Res. 2022;40:56–65.
18. Alfonso-Loeches S, Urena-Peralta JR, Morillo-Bargues MJ, De La Cruz JO, Guerri C. Role of mitochondria ROS generation in ethanol-induced NLRP3 inflammasome activation and cell death in astroglial cells. Front Cell Neurosci. 2014;8:216.
19. Abdelmalik PA, Draghic N, Ling GSF. Management of moderate and severe traumatic brain injury. Transfusion. 2019;59:1529–38.

20. Xiao S, Zhang Y, Liu Z, Li A, Tong W, Xiong X, Nie J, Zhong N, Zhu G, Liu J, Liu Z. Alpinetin inhibits neuroinflammation and neuronal apoptosis via targeting the JAK2/STAT3 signaling pathway in spinal cord injury. CNS Neurosci Ther. 2023;29:1094–108.
21. Mousavi A. CXCL12/CXCR4 signal transduction in diseases and its molecular approaches in targeted-therapy. Immunol Lett. 2020;217:91–115.
22. Isbilir A, Moller J, Arimont M, Bobkov V, Perpina-Viciano C, Hoffmann C, Inoue A, Heukers R, de Graaf C, Smit MJ, et al. Advanced fluorescence microscopy reveals disruption of dynamic CXCR4 dimerization by subpocket-specific inverse agonists. Proc Natl Acad Sci U S A. 2020;117:29144–54.
23. Fang RH, Kroll AV, Gao W, Zhang L. Cell membrane coating nanotechnology. Adv Mater. 2018;30:e1706759.
24. Sun D, Liu K, Li Y, Xie T, Zhang M, Liu Y, Tong H, Guo Y, Zhang Q, Liu H, et al. Intrinsically bioactive manganese-eumelanin nanocomposites mediated antioxidation and anti-neuroinflammation for targeted theranostics of traumatic brain injury. Adv Healthc Mater. 2022;11:e2200517.
25. Grundmann A, Wu CH, Hardwick M, Baillie JK, Openshaw PJM, Semple MG, Bohning D, Pett S, Michael BD, Thomas RH, et al. Fewer COVID-19 neurological complications with dexamethasone and remdesivir. Ann Neurol. 2023;93:88–102.
26. Lim SW, Sung KC, Shiue YL, Wang CC, Chio CC, Kuo JR. Hyperbaric oxygen effects on depression-like behavior and neuroinflammation in traumatic brain injury rats. World Neurosurg. 2017;100:128–37.
27. Bhowmick S, D'Mello V, Caruso D, Wallerstein A, Abdul-Muneer PM. Impairment of pericyte-endothelium crosstalk leads to blood-brain barrier dysfunction following traumatic brain injury. Exp Neurol. 2019;317:260–70.
28. Davis CK, Vemuganti R. Antioxidant therapies in traumatic brain injury. Neurochem Int. 2022;152:105255.
29. Karve IP, Taylor JM, Crack PJ. The contribution of astrocytes and microglia to traumatic brain injury. Br J Pharmacol. 2016;173:692–702.
30. Lee WS, Kang JH, Lee JH, Kim YS, Kim JJ, Kim HS, Kim HW, Shin US, Yoon BE. Improved gliotransmission by increasing intracellular Ca(2+) via TRPV1 on multi-walled carbon nanotube platforms. J Nanobiotechnology. 2022;20:367.
31. Guo R, Fang Y, Zhang Y, Liu L, Li N, Wu J, Yan M, Li Z, Yu J. SHED-derived exosomes attenuate trigeminal neuralgia after CCI of the infraorbital nerve in mice via the miR-24-3p/IL-1R1/p-p38 MAPK pathway. J Nanobiotechnology. 2023;21:458.
32. Zhang B, Wei YZ, Wang GQ, Li DD, Shi JS, Zhang F. Targeting MAPK pathways by naringenin modulates microglia M1/M2 polarization in lipopolysaccharide-stimulated cultures. Front Cell Neurosci. 2018;12:531.
33. Ogino Y, Bernas T, Greer JE, Povlishock JT. Axonal injury following mild traumatic brain injury is exacerbated by repetitive insult and is linked to the delayed attenuation of NeuN expression without concomitant neuronal death in the mouse. Brain Pathol. 2022;32:e13034.
34. Reiprich S, Wegner M. From CNS stem cells to neurons and glia: sox for everyone. Cell Tissue Res. 2015;359:111–24.
35. Simon DW, McGeachy MJ, Bayır H, Clark RS, Loane DJ, Kochanek PM. The far-reaching scope of neuroinflammation after traumatic brain injury. Nat Rev Neurol. 2017;13:171–91.
36. Ye Y, Jin T, Zhang X, Zeng Z, Ye B, Wang J, Zhong Y, Xiong X, Gu L. meisoindigo protects against focal cerebral ischemia-reperfusion injury by inhibiting NLRP3 inflammasome activation and regulating microglia/macrophage polarization via TLR4/NF-κB signaling pathway. Front Cell Neurosci. 2019;13:553.
37. Su P, Wu M, Yin X, Li M, Li Y, Bai M, Wang B, Xu E. Modified Xiaoyao San reverses lipopolysaccharide-induced depression-like behavior through suppressing microglia M1 polarization via enhancing autophagy involved in PI3K/Akt/mTOR pathway in mice. J Ethnopharmacol. 2023;315:116659.
38. Bao Q, Hu P, Xu Y, Cheng T, Wei C, Pan L, Shi J. Simultaneous blood-brain barrier crossing and protection for stroke treatment based on edaravone-loaded ceria nanoparticles. ACS Nano. 2018;12:6794–805.
39. Kim J, Kim HY, Song SY, Go SH, Sohn HS, Baik S, Soh M, Kim K, Kim D, Kim HC, et al. Synergistic oxygen generation and reactive oxygen species scavenging by manganese ferrite/ceria co-decorated nanoparticles for rheumatoid arthritis treatment. ACS Nano. 2019;13:3206–17.
40. Yang Z, Lin P, Chen B, Zhang X, Xiao W, Wu S, Huang C, Feng D, Zhang W, Zhang J. Autophagy alleviates hypoxia-induced blood-brain barrier injury via regulation of CLDN5 (claudin 5). Autophagy. 2021;17:3048–67.
41. Li Y, Liu K, Li C, Guo Y, Fang J, Tong H, Tang Y, Zhang J, Sun J, Jiao F, et al. (18) F-FDG PET combined With MR spectroscopy elucidates the progressive metabolic cerebral alterations after blast-induced mild traumatic brain injury in rats. Front Neurosci. 2021;15:593723.
42. Xie T, Chen X, Fang J, Xue W, Zhang J, Tong H, Liu H, Guo Y, Yang Y, Zhang W. Non-invasive monitoring of the kinetic infiltration and therapeutic efficacy of nanoparticle-labeled chimeric antigen receptor T cells in glioblastoma via 7.0-Tesla magnetic resonance imaging. Cytotherapy. 2021;23:211–22.

Publisher's Note